ROYAL SOCIETY OF CHEMISTRY

COMMUNICATION

Check for updates

Mesoscale superlubric Brownian machine based on 2D graphitic interfaces†

Keren Stein, Gautham Vijayan, Ron Bessler and Elad Koren ![ORCID] *

Brownian motors utilize thermal activation and asymmetric physical interactions to generate directed motion of nanoscale elements in space. On the other hand, structural superlubricity refers to a macroscopic correlated state of nearly vanishing friction due to structural mismatch between sliding interfaces. In fact, the effective sliding barrier in these systems was shown to depend on temperature, manifested by the thermal lubrication phenomenon. Herein, the unique combination of a carefully designed tilted periodic potential landscape and virtually zero friction in 2D layered systems are used to demonstrate mesoscopic superlubric Brownian operation. We perform mechanical shearing of superlubric graphite contacts to examine the influence of velocity on friction and adhesion. Our results show that while friction is virtually independent of velocity below 2500 nm s^{-1}, the adhesion force increases by $\sim$10% with respect to the lowest measured velocity. This indicates that the system can intriguingly exhibit a counterclockwise hysteretic force loop in which a greater amount of energy can be generated once the retraction velocity is set above the protraction velocity, which is explained by utilizing the available thermal energy to reduce adhesion. The ability to realize mesoscopic mechanical systems that can conceptually extract useful mechanical energy by thermal fluctuations can potentially lead to disruptive technologies such as artificial surfaces, in which controlled motion of elements is manifested by manipulated Brownian motion and self-powered actuators with energy harvest capabilities.

1. Introduction

Brownian motors utilize thermal energy and asymmetric physical interactions to generate directed motion in space.[1,2] Analogue to molecular motors found in nature[3,4] (*e.g.* muscles, ions pump *etc.*), several artificial systems were able to utilize

Faculty of Materials Science and Engineering, Technion – Israel Institute of Technology, 3200003 Haifa, Israel. E-mail: eladk@technion.ac.il

† Electronic supplementary information (ESI) available. See DOI: https://doi.org/10.1039/d5mh00495k

New concepts

Brownian motors found in nature and their artificial counterparts utilize thermal energy to generate directed motion in space, which is motivated by an asymmetric or tilted periodic potential landscape amplifying the probability to move towards designated directions. Nevertheless, due to the requirement to maintain shallow potential with respect to temperature and low Raynolds number to neglect inertia, both artificial and biological Brownian machines are inherently limited by their sizes to $\sim$10 nm and are practically functional in liquid environments. In this work, we introduce structural superlubricity (SSL), referring to a state of nearly vanishing friction due to structural mismatch between macroscopically sliding interfaces in solid conditions, to overcome these constraints. In particular, we demonstrate that the combination of a carefully designed tilted periodic potential landscape and virtually zero friction in mesoscale sheared 2D layered graphitic systems can garnered to realize a mesoscale superlubric Brownian actuator.

random thermal fluctuations to achieve directed motion using optical tweezers,[5] organic chemistry[6] and nanopatterning.[7] The directed motion is motivated by an asymmetric or tilted periodic potential landscape amplifying the probability to move towards designated directions.[8] Thus, although the available thermal energy allows the system to explore any possible excited state with equal probability, the presence of asymmetric potential and non-equilibrium conditions results in a distinct bias towards a particular direction. Nevertheless, due to the requirement to maintain shallow potentials with respect to temperature and low Raynolds number to neglect inertia,[4] both artificial and biological Brownian machines are inherently limited by their sizes to $\sim$10 nm and are practically functional in liquid environments. On the other hand, structural superlubricity (SSL)[9–15] refers to a state of nearly vanishing friction due to structural mismatch between macroscopically sliding interfaces in solid conditions, with the potential of considerably reducing energy loss and wear.[16–18] According to theory, SSL is characterized by vanishing static sliding force for infinite incommensurate flat surfaces, where the work done by one atom is fully compensated by the energy gain of another.[9–11] Consequently, the total friction force can completely vanish for

adiabatic conditions that presumably take place at low sliding velocities.[11] 2-dimensional (2D) van der Waals (vdW) layered materials, such as graphene, h-BN and MoS_2, as well as their 1D counterparts (tubular structures) are of particular interest in this regard as they exhibit atomically flat surfaces and weak interlayer interaction.[12–15,19] These systems were successfully shown to exhibit SSL up to centimeter scale dimentions.[20] In the last decade, many studies have considered the influence of different parameters affecting SSL including the dependence on interlayer orientation,[21–24] sliding direction,[25] applied load,[22,26] electric field,[27] contact size,[28–31] temperature[32] and velocity.[22,33–35]

The experimental relation between friction and velocity has been mostly assessed by an atomic force microscope (AFM) tip, providing an experimental assessment of a single asperity system.[35–41] The friction-velocity relation in few-layer graphene has been shown to depend strongly on thickness,[40,41] attributed to puckering,[41–43] or to its interaction with the substrate.[40,41,44] In addition, most studies observe a logarithmic dependence of friction with sliding velocity,[35–41,45] which is consistent with the thermally activated Prandtl-Tomlinson (TAPT) model.[36,46] According to the TAPT model, thermal activation adds energy to the system, which assists in overcoming potential barriers during sliding thereby reducing friction. Thus, slower sliding increases the influence of thermal effects, leading to lower friction. The relation between friction and velocity under SSL conditions, in which the contact area reaches up to few micrometers square, have also attracted significant experimental and theoretical attention.[47,48] Experiments considering the basal plane of graphite,[34] graphite-DLC (diamond-like carbon)[33] and graphite-hBN contacts,[22] mostly show logarithmic dependence of the friction-velocity relations, whereas virtually zero dependence was observed for graphite and graphite-hBN contacts at velocities below 1 μm s^{-1}, which

can presumably be attributed to adiabatic conditions.[11,45] The interlayer adhesion energy (binding energy) of several 2D materials including their heterostructures have also garnered notable attention,[28,49–52] due to their impact on nanoscale actuation,[28] device fabrication, stability and performance.[53,54] In contrast with friction, adhesion is traditionally considered velocity independent, yet experimental and theoretical work on this matter are scarce.[53,55,56] Importantly, the intriguing observation of self-retraction phenomena in graphite demonstrate the ability to almost fully conserve the total energy of the system while repeatedly breaking and repairing the interface.[28,57]

In this work, we demonstrate that the combination of a carefully designed tilted periodic potential landscape and virtually zero friction in sheared 2D layered systems can garnered to realize a mesoscale superlubric Brownian actuator. We start by studying the velocity dependent friction and adhesion of mesoscale 2D graphitic contacts in the superlubricity regime using an AFM setup, similar to our previous work.[23,27,28,58,59] We show that the friction dependence can be divided into two velocity regimes, where friction is virtually independent of velocity below 2500 nm s^{-1} (Regime I), with a following logarithmic increase above this range (Regime II), similar to recent reports.[34,45] Moreover, the increase in friction is solely observed for the onwards direction (exfoliation), whereas no increase in friction is observed for the backwards direction (self-retraction), even up to the highest tested sliding velocity of 125 000 nm s^{-1}. Most intriguingly, by analyzing the adhesion forces at the low velocity regime (Regime I), we observe a continuous increase of up to ∼10%, that does not correspond to an increase in the dissipated energy throughout the exfoliation/retraction processes. Consequently, we propose a generic operational system that can exhibit a counterclockwise hysteretic force loop once the retraction velocity is set above the
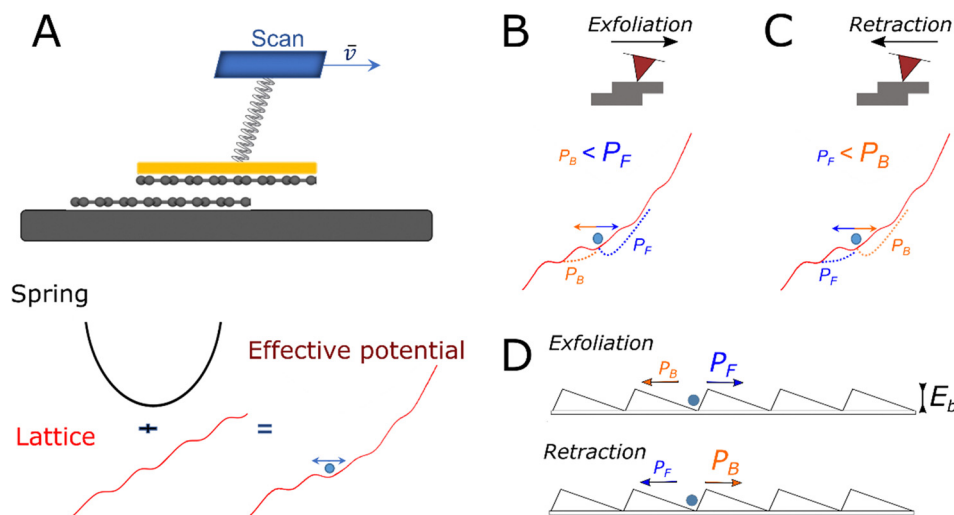

Fig. 1 (A) Schematics of the mesoscale Brownian motor system (top). Potential energies for the spring (parabolic) and graphite lattice (periodic) *vs.* displacement and the combined effective asymmetric potential (bottom). The asymmetric effective potential distribution and the probability to move forward P_F and backward P_B during the exfoliation (B) and retraction (C) processes. (D) Schematics of an asymmetric potential landscape and the probability of a particle to move forward and backward across the energy barrier E_b when temperature $T \sim E_b/k_B$ (thermal energy approaches the energy of the sliding barrier).

protraction velocity allowing to extract a useful amount of mechanical energy. Finally, we present numerical calculations based on force field modelling indicating that slow adiabatic sliding allows to utilize the available thermal energy to reduce adhesion, in agreement with our experimental observations.

The operation principle of the mesoscopic superlubric Brownian motor is schematically illustrated in Fig. 1. The system comprises an actuated bilayer graphene interface, where a simple mechanical spring (representing the AFM tip) is used for laterally shearing the top section with a velocity $\bar{v}$ to reduce the interfacial areal overlap (Fig. 1A). The energy of the AFM spring as a function of distance can be described by a parabola $i.e.$ $U_S = k (x - x_0)^2$ (solid black line, Fig. 1A), where k and $x - x_0$ are the cantilever lateral stiffness and distance away from equilibrium, respectively. The crystalline atomic structure at the interface corresponds to a tilted periodic potential energy (solid red line, Fig. 1A), where the linear trend is attributed to the adhesive forces acting to increase energy as the area overlap reduces. The corresponding asymmetric potential and the probability to move forward P_F and backward P_B during the exfoliation and retraction processes are presented in Fig. 1B and C, respectively. In essence, in both cases there is a statistical preference for moving towards the right direction to release the mechanical tension of the spring. Hence, a larger probability is established for moving forward and backward during the exfoliation and retraction, respectively. The effective potential landscape is somehow analogue to the one presented in Fig. 1D, which is a familiar element in Brownian machines.[1,7] In particular, under certain nonequilibrium conditions it can facilitate an asymmetric probability of a particle to move forward and backward across an energy barrier E_b at $T > 0$ K $i.e.$ $T \sim E_b/k_B$ (thermal energy approaches the energy of the sliding barrier), where k_B is the Bolzman constant.

2. Experimental results

The dependence of adhesion and friction on sliding velocity was studied by means of mechanical manipulation of mesoscale graphitic contacts (Fig. 2A). Graphitic contacts featuring
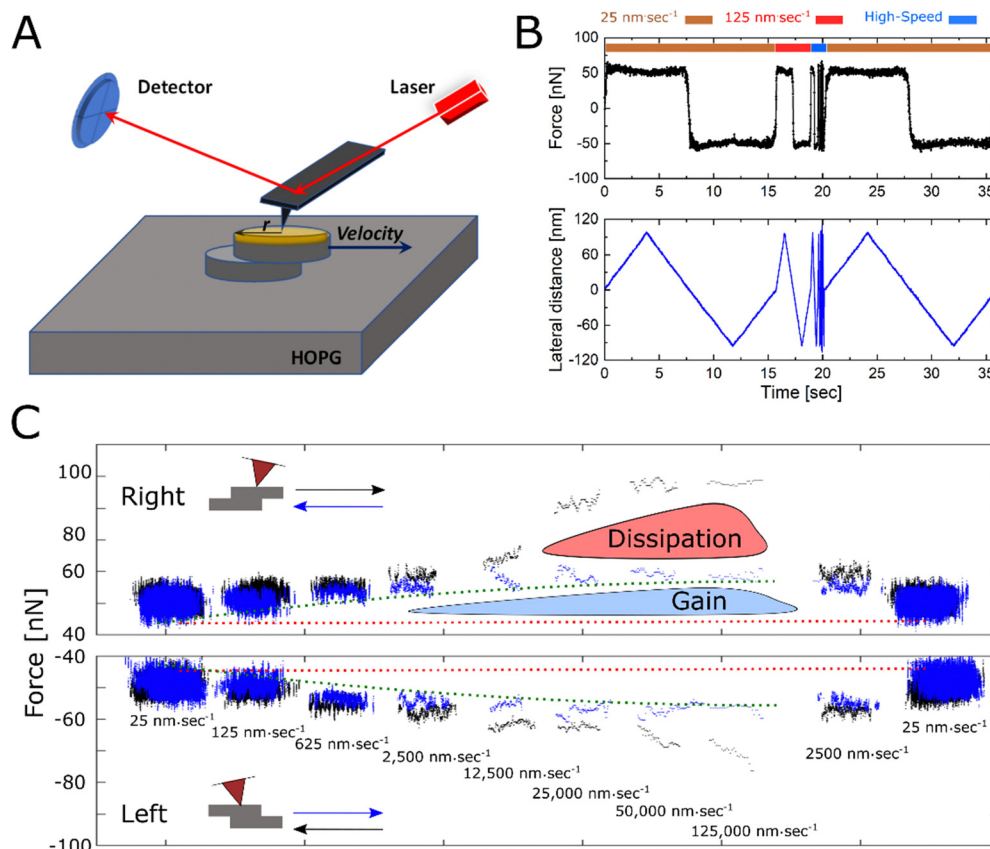

Fig. 2 (A) Schematic description of the experimental setup. The AFM tip is cold-welded to the metal mask on top of the pillar, allowing to induce lateral shearing. The signal retrieved from the deflection of the laser beam represents the force applied by the tip at each point. (B) Measured lateral force (top) and distance (bottom) $versus$ time while shearing the top part of the graphitic mesa structure at different velocities. Visible velocities displayed by the top color bar are 25 nm s^{-1} (brown) and 125 nm s^{-1} (red), while faster cycles of 625, 2500, 12 500, 25 000, 50 000 and 125 000 nm s^{-1} (blue) are more difficult to observe in this timescale. (C) Trace (black) and retrace (blue) force profiles measured at different sliding velocities (profiles are laterally shifted for better visualization). The profiles at the right side for 2500 and 25 nm s^{-1} are repeated at the end of the experiment to confirm that the measured variations in force are not due to setup instabilities. Dashed red (horizontal) and green (non-uniform) lines are added as a guide to the eye to follow the adhesive force variations as a function of sliding velocities. Top (bottom) panel represents the measured forces for the case where the tip is sheared within the right (left) side of the pillar (as indicated by the inset schematics). Dissipation regime at high sliding velocities is marked by the red filled area, whereas the regime in which energy can be gained is marked by the light blue filled area.

cylindrical structures with a typical height of 100 ± 10 nm and a diameter of 210 ± 5 nm were constructed from highly oriented pyrolytic graphite (HOPG) based on a recently presented fabrication method.[23,27,28,58,59] The applied lateral forces induce a shear glide along a single basal plane in the HOPG structure. The lateral force was recorded for sliding velocities of 25 to 125 000 nm s^{-1} along a total distance equal to the mesa radius *i.e.* 100 nm (Fig. 2B). The total shear force is composed of a reversible displacement force due to adhesion and a smaller irreversible friction force characterized by force hysteresis. The small magnitude of the friction (see next section, Fig. 3B) and the small force fluctuations (<20 nN) indicate that the sliding is done under superlubric conditions.[14,28,60] Fig. 2C presents the complete measured set of the lateral force profiles for different sliding velocities within the range of 25 to 125 000 nm s^{-1}. Top (bottom) panel represents the measured forces for the case where the tip is sheared within the right (left) side of the pillar (as indicated by the inset schematics). Initial and final cycles executed at 25 and 2500 nm s^{-1} are virtually

identical in terms of the average force magnitude and fluctuations range, thereby eliminating the influence of possible artifacts related to drift or an induced structural damage to the mesa structure throughout the mechanical actuation. It is clearly evident that the average sliding force for both trace (exfoliation, black profiles) and re-trace (retraction, blue profiles) directions increase (in absolute units) with increasing velocity. Moreover, beyond a lateral velocity of ~2500 nm s^{-1}, the trace/re-trace profiles begin to separate as evidence for increase in dissipated energy (red filled area section). Intriguingly, while all trace (exfoliation) force profiles keep growing with increase in velocity, the re-trace (retraction) profiles saturate along the maximum force magnitude of the lower velocity regime (marked by the dashed green line). This indicates that the increase in friction at high sliding velocities is solely associated with the exfoliation process, whereas retraction introduces virtually zero energy dissipation up to the highest tested velocity *i.e.* 125 000 nm s^{-1}. We attribute this behavior to the intrinsically high self-retraction speed *i.e.* $\sim$ millimeter
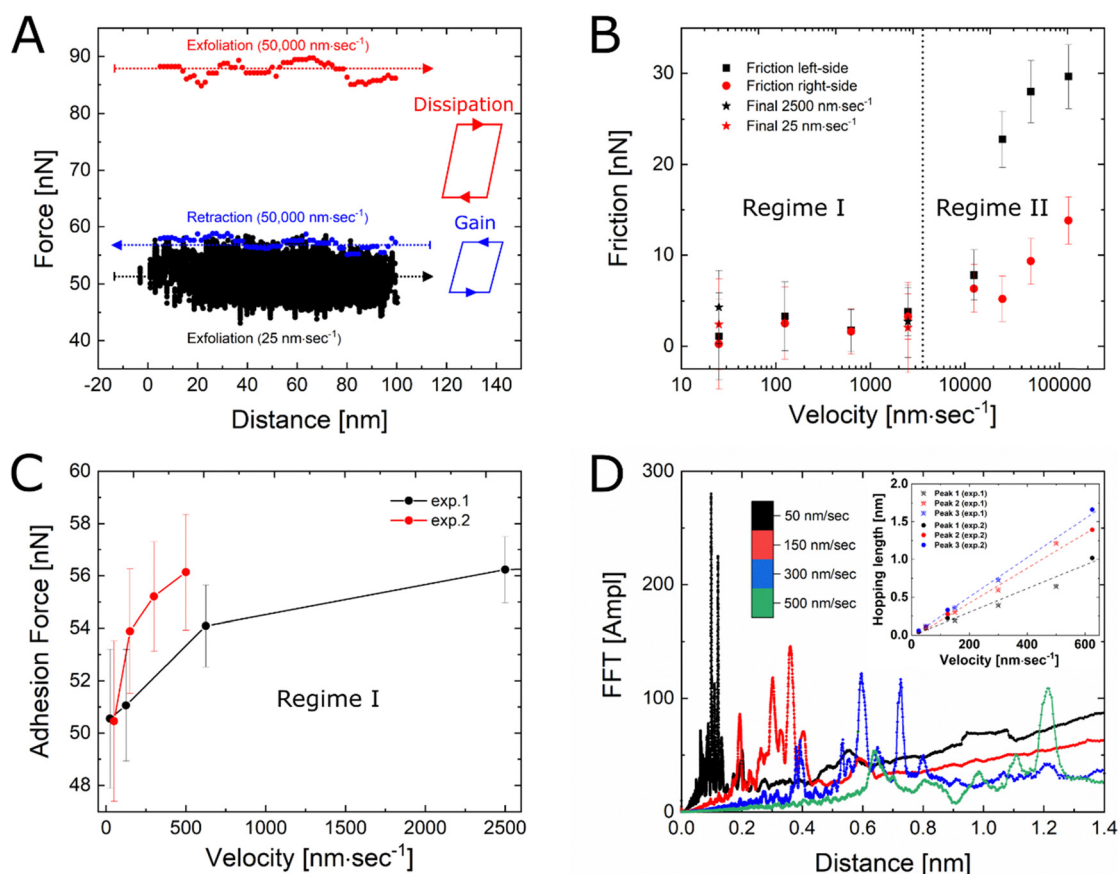

Fig. 3 (A) Measured force *versus* distance profiles for high exfoliation (red symbols) and retraction (blue symbols) velocities and for low exfoliation velocity (black symbols). Inset schematics describe the clockwise dissipative friction loop for high exfoliation and retraction velocities and a counterclockwise hysteretic loop with energy gain for the case of slow exfoliation and fast retraction. (B) Calculated average friction force for different velocities. "left-side" and "right-side" represent the direction to which the pillar is sheared before returning to the center. Friction is effectively constant below 2500 nm s^{-1} (Regime I). The final sliding cycles for 25 and 2500 nm s^{-1} are marked by star symbols (*). (C) Average adhesion force based on two experiments *versus* velocities related to Regime I (below 2500 nm s^{-1}), where friction is virtually zero and independent of the applied velocity. (D) Fast Fourier transformation (FFT) of the measured force profiles for velocities: 50, 150, 300, 500 nm s^{-1}. Peaks represent typical hopping length between two consecutive energy minima (Inset: Three most prominent hopping lengths peaks per velocity. Data includes results from two different experiments *i.e.* exp. 1 and exp. 2.).

per second of sheared graphitic structures in the superlubricity regime.[61] For more information about the evaluation of friction and adhesion in our setup please refer to the ESI.† An intriguing consequence of the observed force *versus* velocity characteristics is that an energy gain *i.e.* counterclockwise hysteretic force loop can be realized by velocity control of the trace and retrace manipulations (light blue filled area section). This is demonstrated by presenting the trace (exfoliation) at low velocity *e.g.* 25 nm s^{-1} and retrace (retraction) at a higher velocity *e.g.* 50 000 nm s^{-1}, where energy can be effectively extracted by the system (black and blue force profiles in Fig. 3A). As will be discussed below, such energy gain is attributed to thermal excitations of the slider allowing to overcome the potential barriers during the exfoliation process (executed at sufficiently low velocity), whereas the retraction performed at high velocity inhibits thermal energy relaxations that would otherwise eliminate energy gain during the retraction.

Fig. 3B and C show the calculated friction and adhesion forces, respectively. The friction force was calculated separately for the displacement of the top mesa structure to the left (black symbols) and right (red symbols) sides with respect to the fully overlap position (*i.e.* top and bottom parts of Fig. 2C). The adhesion was considered as the difference between the average positive force (measured while the mesa was sheared to the left side with respect to pillar center position) and the average negative force (measured while the mesa was sheared to the right with respect to pillar center position) divided by two (see also ESI†). At velocities below 2500 nm s^{-1} (Regime I), the friction force is virtually zero with respect to its standard deviation and with no measurable dependence on velocity, suggesting that the sliding is adiabatic. For velocities above 2500 nm s^{-1} (Regime II), the friction force is characterized by a logarithmic growth, in accordance with previous research.[22,33–35,45] To adequately examine the velocity dependence of the adhesion force, we considered velocities below 2500 nm s^{-1} (Regime I), in which friction is effectively independent of the sliding velocity (Fig. 3C). As demonstrated by the two separate experiments presented in Fig. 3C, the average adhesion force grows by ∼10% with respect to the lowest measured velocity until it saturates.

The influence of velocity on the adhesive forces is rather intriguing, since adhesion is typically considered as a conservative force and therefore independent of velocity.[55,56,62] In fact, our experimental analysis demonstrate the potential to gain useful mechanical energy by velocity modulation. To better understand the intricate atomic interactions at the sliding interface, we perform Fourier transformation to the lateral force *versus* distance profiles, for velocities 50, 150, 300 and 500 nm s^{-1} (Fig. 3D). The observed peaks correspond to the typical hopping length between two consecutive energy minima and are in good agreement with previous report.[28] Interestingly, at higher velocities the profiles become more dispersed and are characterized by longer hopping distances, where the contact overpasses more than one potential barrier per each hopping event. The inset shows the correlation between the hopping length and sliding velocity for the three most prominent peaks of each velocity, where the distance between consecutive

hopping lengths appears to grow linearly with sliding velocity, which is in good agreement with recent observations for a single asperity contact sliding across an MoS$_2$ surface.[63] The observed distinct hopping events and their correlation with velocity indicate that the upper contact acts as a relatively stiff element sliding across a mild potential landscape, suggesting that the system can effectively be described as a single asperity element, in good analogy with the typical description for nanoscale Brownian systems, and where thermal energy can facilitate facile movement across potential barriers.

In order to theoretically support our experimental results, we performed numerical simulations based on the force field theory of Kolmogorov–Crespi for graphitic interfaces.[64] The total potential U_T includes both the lattice interaction energy U_L and the mechanical spring U_S that is used to shear the top graphitic contact, similar to the experimental method:

$$U_T = U_L + U_S = U_L + k(x - x_0)^2 \tag{1}$$

where k is the spring constant representing the cantilever stiffness. In addition, the model includes possible relaxations in both the off-sliding axis Y and the mismatched angle θ due to preferred energetical orientations (see Methods and supplementary sections for more details). For simplicity, we assume rigidity of the surfaces and neglect surface relaxation. This assumption is rather rational under superlubric conditions, where the angularly misfitted interlayer configuration results in a Moiré structure with relatively small domains.[60,65] In addition, out-of-plane distortions are significantly small for macroscopically supported contacts as opposed to single layer sliders.[40] The lattice potential energy is calculated by summing up the individual interactions between the carbon atoms within the contacted layers for each position throughout the slide. The driving force is the cantilever spring that moves at constant velocity. Hence, once the stored energy within the spring overcomes the energy barrier for slide, the equilibrium position x_0 will change. To allow for thermal excitations, we consider the Bolzman exponential occupation probability of higher energetic states. For each path option (x, y, θ) the energy difference $\Delta E_{xy\theta} = E_{xy\theta} - E_0$ between the next ($E_{xy\theta}$) and prior (E_0) configurations is calculated and a path probability $P_{xy\theta} = \exp(-\Delta E_{xy\theta}/(k_B T))$ function is assigned to allow for thermal fluctuations. The actual path is chosen randomly according to the path probability weight. The model thus entails an intrinsic thermally activated randomness. Fig. 4 presents the simulated results for two different velocities of the spring platform. While both Y- and θ-positions present less features of the interfacial lattice interaction for the higher velocity of 0.35 Å s^{-1} in comparison with the slower velocity of 0.025 Å s^{-1} (Fig. 4A), the equilibrium position x_0 for the higher velocity of 0.35 Å s^{-1} shows larger lagging after the x position of the spring platform (Fig. 4B). Hence, we expect that the larger spring extension at higher velocity will correspond to higher spring force. Evidently, the simulated spring force *versus* lateral position is larger for the higher velocity of 0.35 Å s^{-1} and follows the force maximal values of the slower velocity, in agreement with the experimental results (dashed green lines in Fig. 2C). Moreover, the force fluctuations
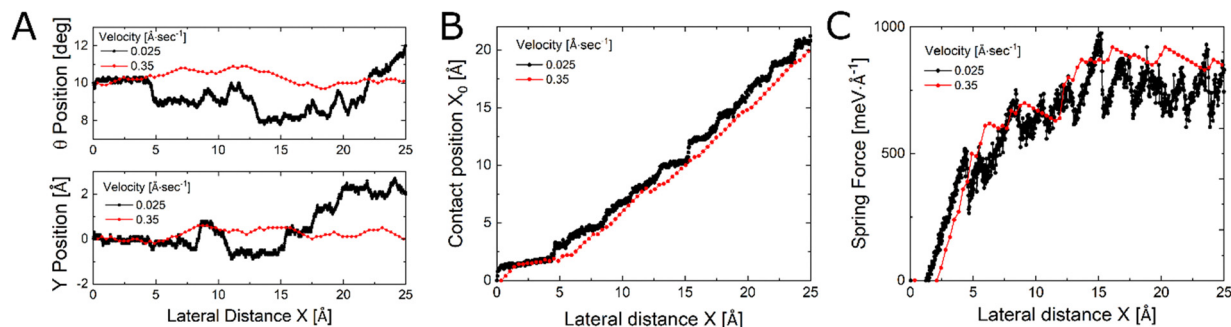
Fig. 4 Simulated results for two different velocities conditions for 100 Å diameter bilayer graphene interface during shearing from the center position (full overlap). The initial misfit angle and the Y-position offset were set to 10 deg and zero, respectively. Temperature is set to 300 K. (A) Y-Position and rotation misfit angle θ during the slide. (B) x_0-position of the top flake during the slide. At low velocity of 0.025 Å s^{-1}, the spring tends to jump forward earlier during the slide and therefore it is overall more relaxed compared to high velocity case of 0.35 Å s^{-1}. (C) Force *versus* distance profile, where the force profile of the higher velocity case follows the maximal values of the low velocity case, in agreement with the experimental results.

for the higher velocity case often features hopping over two potential barriers, in good correspondence with the experimental results (Fig. 3D). Similar results for initial angular mismatched configurations of 20 and 30 deg are included in the

ESI.† In order to better understand the origin of the velocity dependent characteristics, we consider next the effect of temperature on the sliding force characteristics. Fig. 5 presents simulated shearing results at two different temperature
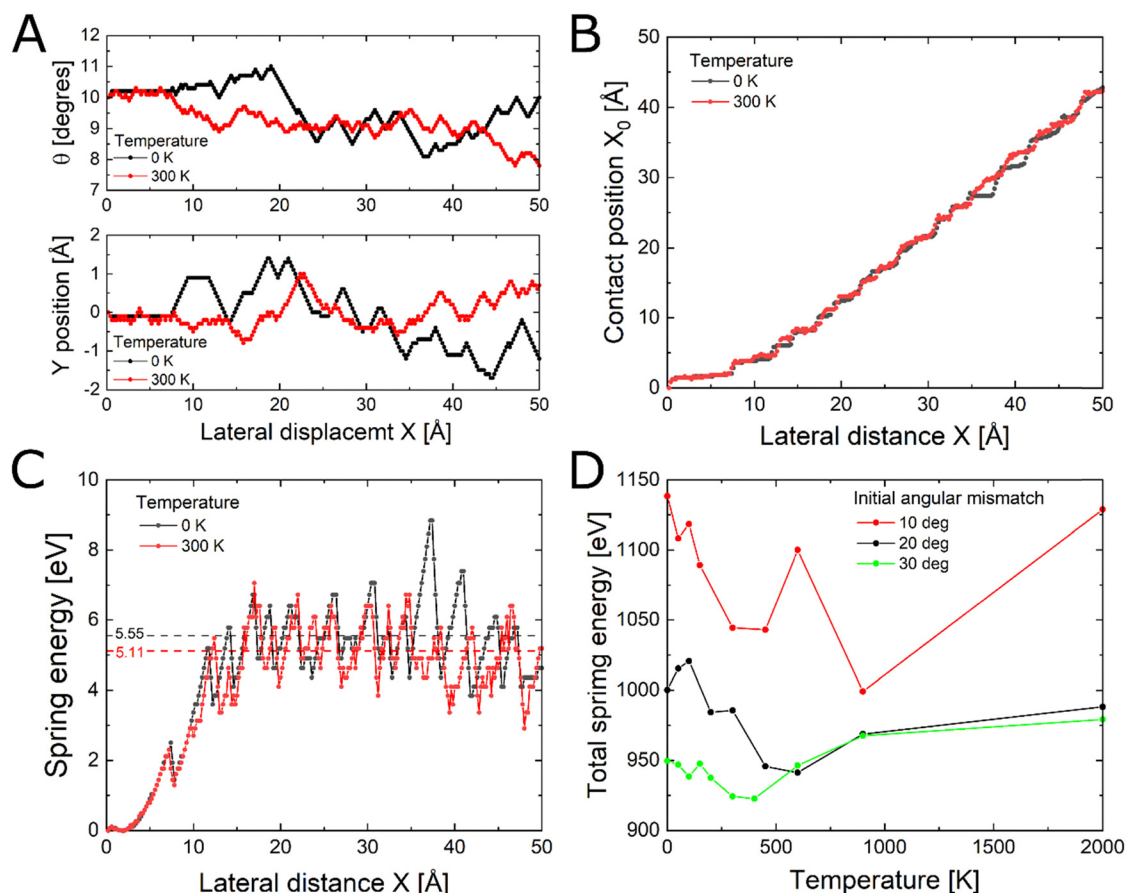

Fig. 5 Simulated results for different temperature conditions for 100 Å diameter bilayer graphene interface during shearing from the center position (full overlap). The initial misfit angle and the Y-position offset were set to 10 deg and zero, respectively. (A) Y-Position and rotation misfit angle θ during the slide. (B) x_0-position of the top flake during the slide. At 300 K, the spring tends to jump forward earlier during the slide and therefore it is overall more relaxed compared to 0 K. (C) Energy of the moving spring *versus* distance. Average values are marked by the dashed lines for each temperature (average is considered between 15–50 Å). (D) Total energy of the springs during the slide *versus* temperature for three different initial angular mismatched conditions.

conditions of 0 and 300 K. We present the off-slide axis Y- and misfit angle θ throughout the slide (Fig. 5A). Due to the higher temperature, the sliding at 300 K is less restricted to the minimum energy path. More intriguingly, the interfacial equilibrium position x_0 presents earlier movements forward for the higher temperature conditions, which indicates that the spring is effectively less stretched on average and thus consumes less energy during the slide (Fig. 5B). Fig. 5C present the spring energy U_S during the slide for the two different temperature conditions. The average spring energy (dashed horizontal lines in Fig. 5C) throughout the slide (average is considered between lateral distance of 15–50 Å) is slightly lower for the higher temperature case, indicating that thermal energy plays an important role in the reduction of the spring energy and consequently the effective adhesion energy of the graphitic interface. Fig. 5D presents the total spring energy *versus* temperature for three initial angular mismatched configurations, in which a clear minimum in energy is evident for all three cases. Interestingly, the minimal energy point shifts to a higher temperature as the angular mismatch configuration reduces, presumably due to the relatively larger potential barrier of lower angular mismatched configurations. It is important to note that it is rather counterintuitive that at higher temperatures the cantilever will be less stretched on average than at lower temperatures, as one would naively expect that the available thermal energy will facilitate the excitation of the spring to higher energy states *i.e.* larger tension. Indeed, at much higher temperatures thermal energy excites the spring to higher energy states leading to larger average tension and increasing energy consumption.

3. Conclusions

This study demonstrates the potential for mesoscopic superlubric Brownian operation through the unique combination of a tilted periodic potential landscape and near-zero friction in 2D layered systems. In particular, velocity dependent mechanical shearing experiments on superlubric graphite contacts reveal that while friction remains nearly constant at velocities below 2500 nm s^{-1}, adhesion forces increase by approximately 10% compared to the lowest observed velocity. Hence, the conservative nature of the adhesion force intriguingly suggests that the system can exhibit a counterclockwise hysteretic force loop, enabling greater energy generation when the retraction velocity surpasses the protraction velocity. Furthermore, analysis of hopping distance and its correlation with velocity indicates that the mesoscopic sliding contact behaves as a rigid single asperity element, akin to nanoscale Brownian systems, where thermal energy can facilitate smooth movement across potential barriers. The ability to utilize thermal energy for overcoming potential barriers in mesoscale sliding systems opens up exciting prospects for macroscopic mechanical systems that can conceptually harness mechanical energy through thermal fluctuations. Such advancements could pave the way for innovative technologies, including artificial surfaces with controlled element motion driven by manipulated Brownian

motion and self-powered actuators featuring energy-harvesting capabilities.

4. Methods

4.1. Fabrication and shearing procedure

The graphite structures were fabricated from HOPG by means of reactive ion etching (RIE), using structured Pd–Au metal layers as self-aligned shadow masks. Nanomanipulation of individual nano-sized graphitic contacts was performed by an AFM in an N$_2$ filled glovebox (H$_2$O and O$_2$ content < 1 ppm). Cold-welding of a Pt/Ir metal-coated AFM tip to the metal on top of the mesa was established by applying a normal force and electrical voltage pulse of 50 nN and 4 V, respectively, for 1 s. The strong mechanical contact formed allows to apply lateral shear forces inducing a shear glide along a single basal plane in the HOPG structure. During the lateral manipulation of the graphitic mesas the normal force was kept below 5 nN.

4.2. Lateral force constant calibration

We use the adhesion energy of graphite $\sigma = 0.227$ [J m^{-2}] to calibrate the lateral force constant of the AFM cantilever.[28] Thus, we can directly use the graphite contact radii, r, to compute the measured lateral force *i.e.* $F = 2\sigma r$. The friction is calculated based on the difference in average force for trace and re-trace sliding directions. The adhesion is calculated as the difference between the average positive force (measured while the mesa was sheared to the left, including both trace and re-trace profiles) and the average negative force (measured while the mesa was sheared to the right, including both trace and re-trace profiles) divided by two.

4.3. Simulations

The interfacial potential energy is calculated according to the Kolmogorov–Crespi model.[64] The hexagonal graphite lattice had an inter-atomic distance of $a = 1.42$ Å and lattice parameter of 2.46 Å. The circular graphite flakes had a diameter of 100 Å, and the initial non-commensurate rotation angle was set to 10, 20 and 30 degrees. The simulation begins with the fully overlap position of the bilayer graphene interface and then the top flake is pulled to the right by the spring for a lateral distance of 25 Å and 50 Å for the velocity and temperature dependent analysis, respectively. For each step the preferred interlayer configuration (account by the Bolzman distribution) was set by adjusting the x_0, y and θ coordinates relative to the previous condition with a maximum change of ±0.4 Å, ±0.2 Å and ±0.2 degrees, respectively (discretized steps of 0.1 Å along the x and y axes and 0.1^0 for rotation). The spring base velocity in the x - direction was kept constant *i.e.* 0.2 Å s^{-1} for the temperature dependent analysis. The spring constant k was set to 100 [meV Å^{-2}].

Data availability

The data supporting this article have been included as part of the ESI.†

Conflicts of interest

The authors declare no competing interests.

Acknowledgements

References

1 P. Reimann, *Phys. Rep.*, 2002, **361**, 57–265.

2 P. Hänggi and F. Marchesoni, *Rev. Mod. Phys.*, 2009, **81**, 387–442.

3 R. Ait-Haddou and W. Herzog, *Cell Biochem. Biophys.*, 2003, **38**, 191–213.

4 R. Ait-Haddou and W. Herzog, *J. Electromyogr. Kinesiol.*, 2002, **12**, 435–445.

5 L. P. Faucheux, L. S. Bourdieu, P. D. Kaplan and A. J. Libchaber, *Phys. Rev. Lett.*, 1995, **74**, 1504–1507.

6 J. V. Hernández, E. R. Kay and D. A. Leigh, *Science*, 2004, **306**, 1532–1537.

7 M. J. Skaug, C. Schwemmer, S. Fringes, C. D. Rawlings and A. W. Knoll, *Science*, 2018, **359**, 1505–1508.

8 P. Reimann, C. Van den Broeck, H. Linke, P. Hänggi, J. M. Rubi and A. Pérez-Madrid, *Phys. Rev. Lett.*, 2001, **87**, 010602.

9 M. Peyrard and S. Aubry, *J. Phys. C Solid State Phys.*, 1983, **16**, 1593–1608.

10 M. Hirano, K. Shinjo, R. Kaneko and Y. Murata, *Phys. Rev. Lett.*, 1991, **67**, 2642–2645.

11 K. Shinjo and M. Hirano, *Surf. Sci.*, 1993, **283**, 473–478.

12 J.-M. Martin, in *Superlubricity*, ed. A. Erdemir and J.-M. Martin, Elsevier Science B.V., Amsterdam, 2007, pp. 207–225.

13 P. E. Sheehan and C. M. Lieber, *Science*, 1996, **272**, 1158–1161.

14 M. Dienwiebel, G. S. Verhoeven, N. Pradeep, J. W. M. Frenken, J. A. Heimberg and H. W. Zandbergen, *Phys. Rev. Lett.*, 2004, **92**, 126101.

15 Z. Liu, J. Yang, F. Grey, J. Z. Liu, Y. Liu, Y. Wang, Y. Yang, Y. Cheng and Q. Zheng, *Phys. Rev. Lett.*, 2012, **108**, 205503.

16 K. Holmberg and A. Erdemir, *Friction*, 2017, **5**, 263–284.

17 K. Holmberg, P. Andersson, N.-O. Nylund, K. Mäkelä and A. Erdemir, *Tribol. Int.*, 2014, **78**, 94–114.

18 J. A. Williams and H. R. Le, *J. Phys. Appl. Phys.*, 2006, **39**, R201–R214.

19 G. Vijayan and E. Koren, *Nano Lett.*, 2024, **24**, 8973–8978.

20 R. Zhang, Z. Ning, Y. Zhang, Q. Zheng, Q. Chen, H. Xie, Q. Zhang, W. Qian and F. Wei, *Nat. Nanotechnol.*, 2013, **8**, 912–916.

21 R. Ribeiro-Palau, C. Zhang, K. Watanabe, T. Taniguchi, J. Hone and C. R. Dean, *Science*, 2018, **361**, 690–693.

22 Y. Song, D. Mandelli, O. Hod, M. Urbakh, M. Ma and Q. Zheng, *Nat. Mater.*, 2018, **17**, 894–899.

23 E. Koren, I. Leven, E. Lörtscher, A. Knoll, O. Hod and U. Duerig, *Nat. Nanotechnol.*, 2016, **11**, 752–757.

24 E. Koren and U. Duerig, *Phys. Rev. B*, 2016, **93**, 201404.

25 Y. Song, J. Wang, Y. Wang, M. Urbakh, Q. Zheng and M. Ma, *Phys. Rev. Mater.*, 2021, **5**, 084002.

26 S.-W. Liu, H.-P. Wang, Q. Xu, T.-B. Ma, G. Yu, C. Zhang, D. Geng, Z. Yu, S. Zhang, W. Wang, Y.-Z. Hu, H. Wang and J. Luo, *Nat. Commun.*, 2017, **8**, 14029.

27 R. Bessler, U. Duerig and E. Koren, *Nanoscale Adv.*, 2019, **1**, 1702–1706.

28 E. Koren, E. Lörtscher, C. Rawlings, A. W. Knoll and U. Duerig, *Science*, 2015, **348**, 679–683.

29 D. Dietzel, M. Feldmann, U. D. Schwarz, H. Fuchs and A. Schirmeisen, *Phys. Rev. Lett.*, 2013, **111**, 235502.

30 J. Wang, W. Cao, Y. Song, C. Qu, Q. Zheng and M. Ma, *Nano Lett.*, 2019, **19**, 7735–7741.

31 R. Yaniv and E. Koren, *Adv. Funct. Mater.*, 2019, **0**, 1901138.

32 D. Mandelli, W. Ouyang, O. Hod and M. Urbakh, *Phys. Rev. Lett.*, 2019, **122**, 076102.

33 Y. Gongyang, W. Ouyang, C. Qu, M. Urbakh, B. Quan, M. Ma and Q. Zheng, *Friction*, 2020, **8**, 462–470.

34 C. Qu, K. Wang, J. Wang, Y. Gongyang, R. W. Carpick, M. Urbakh and Q. Zheng, *Phys. Rev. Lett.*, 2020, **125**, 126102.

35 Y. Liu, K. Wang, Q. Xu, J. Zhang, Y. Hu, T. Ma, Q. Zheng and J. Luo, *ACS Appl. Mater. Interfaces*, 2020, **12**, 43167–43172.

36 E. Gnecco, R. Bennewitz, T. Gyalog, Ch Loppacher, M. Bammerlin, E. Meyer and H.-J. Güntherodt, *Phys. Rev. Lett.*, 2000, **84**, 1172–1175.

37 E. Riedo, E. Gnecco, R. Bennewitz, E. Meyer and H. Brune, *Phys. Rev. Lett.*, 2003, **91**, 084502.

38 K. B. Jinesh, S. Yu Krylov, H. Valk, M. Dienwiebel and J. W. M. Frenken, *Phys. Rev. B: Condens. Matter Mater. Phys.*, 2008, **78**, 155440.

39 L. Jansen, H. Hölscher, H. Fuchs and A. Schirmeisen, *Phys. Rev. Lett.*, 2010, **104**, 256101.

40 C. Lee, Q. Li, W. Kalb, X.-Z. Liu, H. Berger, R. W. Carpick and J. Hone, *Science*, 2010, **328**, 76–80.

41 F. Ptak, C. M. Almeida and R. Prioli, *Sci. Rep.*, 2019, **9**, 14555.

42 A. Smolyanitsky, J. P. Killgore and V. K. Tewary, *Phys. Rev. B: Condens. Matter Mater. Phys.*, 2012, **85**, 035412.

43 S. Li, Q. Li, R. W. Carpick, P. Gumbsch, X. Z. Liu, X. Ding, J. Sun and J. Li, *Nature*, 2016, **539**, 541–545.

44 Q. Li, C. Lee, R. W. Carpick and J. Hone, *Phys. Status Solidi B*, 2010, **247**, 2909–2914.

45 Y. Song, X. Gao, A. Hinaut, S. Scherb, S. Huang, T. Glatzel, O. Hod, M. Urbakh and E. Meyer, *Nano Lett.*, 2022, **22**, 9529–9536.

46 Y. Sang, M. Dubé and M. Grant, *Phys. Rev. Lett.*, 2001, **87**, 174301.

47 O. Hod, E. Meyer, Q. Zheng and M. Urbakh, *Nature*, 2018, **563**, 485–492.

48 J. Wang, A. Khosravi, A. Vanossi and E. Tosatti, *Rev. Mod. Phys.*, 2024, **96**, 011002.

49 Z. Liu, J. Z. Liu, Y. Cheng, Z. Li, L. Wang and Q. Zheng, *Phys. Rev. B: Condens. Matter Mater. Phys.*, 2012, **85**, 205418.

50 W. Wang, S. Dai, X. Li, J. Yang, D. J. Srolovitz and Q. Zheng, *Nat. Commun.*, 2015, **6**, 7853.

51 B. Rasche, J. Brunner, T. Schramm, M. P. Ghimire, U. Nitzsche, B. Büchner, R. Giraud, M. Richter and J. Dufouleur, *Nano Lett.*, 2022, **22**, 3550–3556.

52 J. Wang, D. C. Sorescu, S. Jeon, A. Belianinov, S. V. Kalinin, A. P. Baddorf and P. Maksymovych, *Nat. Commun.*, 2016, **7**, 13263.

53 H. Rokni and W. Lu, *Nat. Commun.*, 2020, **11**, 5607.

54 M. Xia, C. Liang, Z. Cheng, R. Hu and S. Liu, *Phys. Chem. Chem. Phys.*, 2019, **21**, 1217–1223.

55 C. Qu, W. Cao, B. Liu, A. Wang, F. Xie, M. Ma, W. Shan, M. Urbakh and Q. Zheng, *J. Phys. Chem. C*, 2019, **123**, 11671–11676.

56 L. Gigli, S. Kawai, R. Guerra, N. Manini, R. Pawlak, X. Feng, K. Müllen, P. Ruffieux, R. Fasel, E. Tosatti, E. Meyer and A. Vanossi, *ACS Nano*, 2019, **13**, 689–697.

57 Q. Zheng, B. Jiang, S. Liu, Y. Weng, L. Lu, Q. Xue, J. Zhu, Q. Jiang, S. Wang and L. Peng, *Phys. Rev. Lett.*, 2008, **100**, 067205.

58 D. Dutta, A. Oz, O. Hod and E. Koren, *Nat. Commun.*, 2020, **11**, 4746.

59 A. Oz, D. Dutta, A. Nitzan, O. Hod and E. Koren, *Adv. Sci.*, 2022, **9**, 2102261.

60 E. Koren and U. Duerig, *Phys. Rev. B*, 2016, **94**, 045401.

61 J. Yang, Z. Liu, F. Grey, Z. Xu, X. Li, Y. Liu, M. Urbakh, Y. Cheng and Q. Zheng, *Phys. Rev. Lett.*, 2013, **110**, 255504.

62 Z. Chen, M. R. Vazirisereshk, A. Khajeh, A. Martini and S. H. Kim, *J. Phys. Chem. Lett.*, 2019, **10**, 6455–6461.

63 Y. Song, J. Wang, A. Hinaut, S. Scherb, S. Huang, T. Glatzel, E. Tosatti and E. Meyer, *Phys. Rev. Lett.*, 2024, **133**, 136201.

64 A. N. Kolmogorov and V. H. Crespi, *Phys. Rev. B: Condens. Matter Mater. Phys.*, 2005, **71**, 235415.

65 C. R. Woods, L. Britnell, A. Eckmann, R. S. Ma, J. C. Lu, H. M. Guo, X. Lin, G. L. Yu, Y. Cao, R. V. Gorbachev, A. V. Kretinin, J. Park, L. A. Ponomarenko, M. I. Katsnelson, Yu. N. Gornostyrev, K. Watanabe, T. Taniguchi, C. Casiraghi, H.-J. Gao, A. K. Geim and K. S. Novoselov, *Nat. Phys.*, 2014, **10**, 451–456.